Applied Thermal Engineering 216 (2022) 118994

Contents lists available at ScienceDirect

Applied Thermal Engineering

journal homepage: www.elsevier.com/locate/apthermeng

# Development of a latent heat thermal energy storage unit for the exhaust of a recuperated solar-dish Brayton cycle

G. Humbert [a], C. Roosendaal [b], J.K. Swanepoel [b], H.M. Navarro [a], W.G. Le Roux [b], A. Sciacovelli [a,*]

[a] Birmingham Centre for Energy Storage, University of Birmingham, Birmingham, United Kingdom
[b] Department of Mechanical and Aeronautical Engineering, University of Pretoria, South Africa

A B S T R A C T

Solar air Brayton cycles can provide heat and power to small communities with no access to the national grid. However, the temporal mismatch between the energy supply and demand can limit the amount of solar energy successfully transferred to the user. To increase this solar utilization factor, a high-temperature latent heat thermal energy storage unit for temperatures of up to 750 K, dedicated to a solar air Brayton cycle, is designed and tested under realistic operating conditions. The storage unit is charged employing the cycle exhaust and discharged after sunset to serve domestic heating applications. In agreement with the identified operating conditions, four storage material candidates are shortlisted and characterized. Thus, the so-called solar salt was selected as the most suitable material by means of 3D numerical analysis to meet a series of performance, durability, cost, and compactness requirements. The proposed latent heat thermal energy storage device was tested with 151 kg of solar salt and allowed for the storage of up to 17.5 kWh in a 10 h charging time. Overall, the numerical and experimental results reported in this work demonstrate the feasibility of the proposed device as a cost-effective and durable thermal storage solution in small-scale solar air Brayton cycles.

## 1. Introduction

Small-scale solar air Brayton cycles can be used to provide heat and power in remote locations with no access to the national grid. In the last decades, several research projects successfully demonstrated the potential of such systems. For example, NASA tested a 10 $kW_{el}$ closed Brayton cycle coupled with a solar dish, with measured thermal efficiencies of above 30% for an inlet turbine temperature of around 1100 K [1]. More recently, Dickey et al. [2] reported on a larger scale (24 $kW_{el}$) recuperated solar Brayton cycle, with thermal efficiencies of around 12%.

However, in such systems, the full exploitation of the solar energy contribution remains hampered by the temporal mismatch between energy supply and energy demand [3]. In this regard, thermal energy storage (TES) technologies are typically adopted to maximize the amount of captured solar energy that can be transferred to the user [4]. In particular, given the required compactness of small-scale solar air Brayton cycles, the integration of latent heat thermal energy storage (LHTES) units has recently attracted researchers' attention. LHTES units rely on phase change materials (PCMs) to deliver or retrieve thermal energy at a nearly constant temperature. In addition, compared to the traditional sensible heat storage (SHS) systems, LHTES units present larger theoretical energy storage densities. In the framework of the OMSOP project [5], phase change materials have been integrated into solar receivers with the aim to mitigate the thermal fluctuations deriving from the variable weather conditions during the day, and thus to allow for more stable turbine inlet temperatures. In fact, in the instance of air Brayton cycles, turbine inlet temperature variations in the range of ± 10 K from the design point have been tested to lead to a thermal efficiency reduction up to −8 % [6]. With the same finality, Bashir et al. [7] investigated the most suitable PCM selection for a solar receiver operated at temperatures above 1100 K. A systematic screening was performed to derive four material candidates and the receiver dynamic thermal performance was predicted by numerical modeling for each of the selected material candidates. The use of a metallic PCM, the MgSi (56–44 $\%_{wt}$), was predicted to maintain the air outlet temperature above a selected threshold of 1100 K for>30 min in the absence of impinging solar flux, out-performing all the other material candidates investigated. In the context of lower receiver operational temperature (1000 K), Cameron et al. [8] proposed LiF as PCM and Columbium-1-Zirconiu as containment material. Le Roux and Sciacovelli [9] maximized the thermal efficiency of solar Brayton cycles by properly selecting off-the-shelf turbochargers and recuperator geometries. Besides, the use of metallic phase change materials around a coiled tube solar receiver was proposed and assessed, observing the most suitable material selection to vary with the turbocharger selection. The highest thermal efficiency was achieved in the instance of MgSi as PCM, for which a thermal efficiency

* Corresponding author.
*E-mail address:* A.Sciacovelli@bham.ac.uk (A. Sciacovelli).

https://doi.org/10.1016/j.applthermaleng.2022.118994
Received 30 January 2022; Received in revised form 31 May 2022; Accepted 7 July 2022
Available online 26 July 2022

**Nomenclature**

*Abbreviations*

| | |
|---|---|
| BDF | Backward Differentiation Formula |
| DSC | Differential scanning calorimetry |
| HT | High-temperature |
| HTF | Heat transfer fluid |
| LFA | Laser Flash Technique |
| LHTES | Latent heat thermal energy storage |
| LT | Low-temperature |
| PCM | Phase change material |
| TES | Thermal energy storage |

*Symbols*

| | |
|---|---|
| $\Delta T_m$ | Melting range [K] |
| $c_p$ | Specific heat [J/kg/K] |
| $E$ | Energy [kWh] |
| $f$ | Liquid fraction [-] |
| $h$ | Enthalpy [J/kg] |
| $H$ | Deterioration rate [mm/year] |
| $h_{conv}$ | Convective heat transfer coefficient [W/m$^2$/K] |
| $h_{global}$ | Global heat transfer coefficient [W/m$^2$/K] |
| $k$ | Thermal Conductivity [W/m/K] |
| $L$ | Latent heat [J/kg] |
| $L_{ins}$ | Insulation thickness [m] |
| $m$ | Mass [kg] |
| $\dot{m}$ | Mass flow [kg/s] |
| $p$ | Pressure [Pa] |
| $SOC$ | State of charge [-] |
| $t$ | Time [s] |
| $T$ | Temperature [K] |
| $\boldsymbol{u}$ | Velocity [m/s] |

*Greek symbols*

| | |
|---|---|
| $\mu$ | Dynamic viscosity [Pa•s] |
| $\rho$ | Density [kg/m$^3$] |

*Subscripts*

| | |
|---|---|
| *0* | Initial |
| *c* | Charge |
| *d* | Discharge |
| *in* | Inlet |
| *m* | Melting |
| *out* | Outlet |
| *th* | Theoretical |

*Superscript*

| | |
|---|---|
| – | Average value |

increase up to + 14.0% was predicted compared to the other design cases considered. Furthermore, the most suitable PCM is found to differ depending on the selected turbocharger, thus highlighting the importance of fit-for-purpose material selection strategies to achieve maximum performance.

Besides the mitigation of the solar flux oscillations, several studies focused on the use of TES systems in solar turbines to increase the solar fraction utilization factor. With this intention, Amsbeck et al. [10] investigated the use of a pressurized pebble-bed sensible heat storage. In the study, the SHS unit was charged by diverting the hot air stream exiting the receiver during low demand times so that a larger amount of solar energy could be fed into the turbine when requested. Due to the SHS integration, the turbine inlet temperature was reduced from 1223 K to 1073 K, with a consequent turbine efficiency reduction of 6.3%. Nonetheless, the solar share of the solar-hybrid microturbine system was enhanced from 25% to 82%. In more recent years, Klein et al. [11] investigated the optimal configuration for a 1.55 $MW_{th}$ alumina packed bed unit integrated into a similar energy system, further increasing the solar utilization factor to 85%.

Large thermal content pertains to the solar air Brayton exhaust, e.g. between 550 and 750 K reported by De Wet et al. [12]. However, the direct integration of such exhaust as the heat source for the Brayton cycle is unfeasible, as Stine and Harrigan [13] determined a minimum temperature of 753 K for the operation of Brayton cycles. Nonetheless, TES units are adopted in the literature to serve secondary cycles thanks to the solar air Brayton cycle exhaust. In the instance of a 5 $MW_{el}$ plant, Ozturk et al. [14] studied the use of a rock bed thermal storage to serve a Rankine cycle operated independently from the sun's availability. The SHS unit was charged during the day in a 4 h time and allowed the steam cycle to run for 12 h. However, low exergy efficiencies were estimated due to the high temperature of the heat source and the relatively low temperature of the targeted application. For a similar plant layout, Allen et al. [15] predicted a 24 × $10^3$ $m^3$ rock bed storage to allow for a 10 h continuous operation of a 25 $MW_{el}$ steam turbine exploiting the exhaust of a 100 $MW_{el}$ gas turbine. However, in the framework of small-scale power production (<10 $kW_{el}$, <40 $kW_{th}$), the use of secondary power cycles might lead to excessive investment and maintenance costs [16]. A cost-effective alternative is the integration of LHTES units to serve heating applications when necessary, such as domestic hot water production and space heating [17]. In this instance, LHTES units becomes key to address evening peaks in heating demand, which cannot be directly satisfied by solar systems.However, to the best of the authors' knowledge, no literature studies have been devoted to the integration of small-scale solar air Brayton cycles with thermal energy storage devices for such an aim. Besides, the vast majority of the aforementioned literature works focused on the prediction and optimization of design concepts, often neglecting key design challenges emerging during the detailed design and manufacturing of high-temperature LHTES units. Therefore, the main objective of this work is the demonstration of the technical feasibility of a LHTES sub-system integrated into a 3 $kW_{el}$ solar air Brayton cycle. Such an objective is achieved by (i) the selection and characterization of PCM candidates, (ii) the performance predictions of a fit-for-purpose LHTES device operated with the shortlisted storage materials and (iii) the manufacturing and testing of the proposed storage sub-system operated with the most suitable PCM.

### 1.1. Novelty and originality of this work

This work proposes a novel high-temperature LHTES unit integrated into small-scale solar air Brayton cycle; in doing so, the manuscript reports the key findings regarding the development, testing and validation of the novel LHTES unit Unique to this work, the proposed storage subsystem is adopted to recover heat from the cycle exhaust gas to serve heating applications after sunset. With such an aim, the work proposes to place the LHTES unit is downstream the power cycle, thus with avoiding negative impact on the on the solar air Brayton cycle performance. As a benefit, the storage subsystem integration allows for an increase of the system solar fraction, as a larger part of the captured solar energy can be effectively transferred to the user during periods of high-demand., Besides the demonstrating the feasibility of the LHTES unit performance testing under realistic operating conditions, this work tackles the need for cost-effective and durable solutions, with both these design aspects typically overlooked in the examined literature. Therefore, The proposed end-to-end development of the LHTES unit also addresses and systematically accounts for the design changes necessary to advance the initial LHTES concept to the actual prototype, accounting

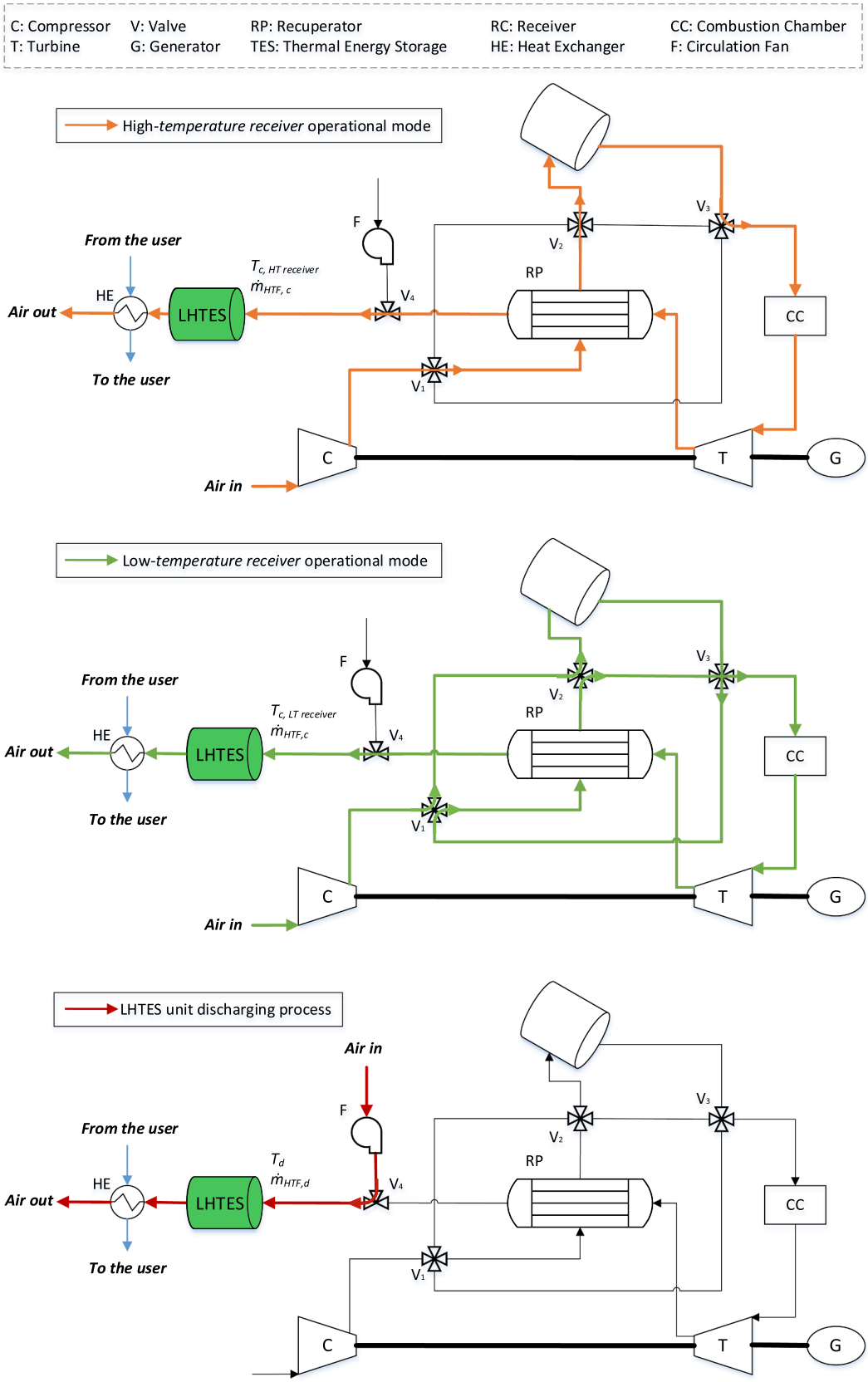


**Fig. 1.** Solar air Brayton cycle layout and investigated operational modes: top for *high-temperature receiver* operational mode; center for *low-temperature receiver* operational mode and bottom for the LHTES unit discharging process. The switch between the operational modes is obtained by means of control valves.

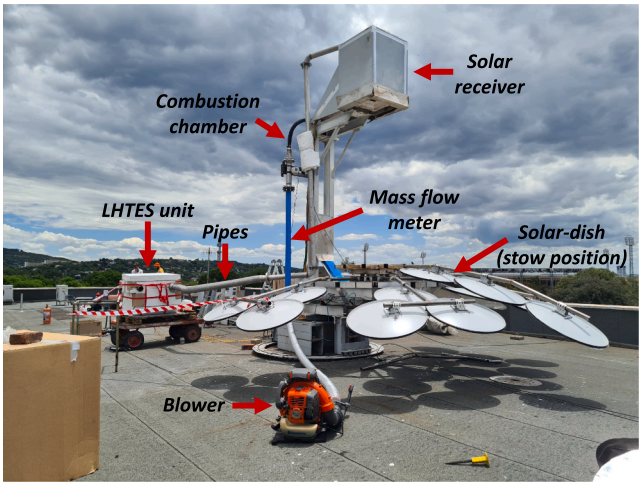


**Fig. 2.** Picture of the LHTES unit sub-system integrated with the solar receiver designed for and of the small-scale solar air Brayton cycle setup (being developed at the University of Pretoria) [20].

for manufacturing and assembly aspects already during the design of LHTES units. Overall, the design approach and design guidelines reported in this work can be extended to the integration of LHTES units in other thermal energy systems, ultimately contributing to the technology advancement.

## 2. System description

### 2.1. Solar air Brayton cycle with integrated LHTES unit

The layout of the hybrid solar air Brayton cycle with the integrated LHTES unit investigated in this work is presented in Fig. 1. The air entering the cycle is compressed by a radial compressor (C) powered by a turbine (T), which is then used to produce shaft power for the generator (G) unit. A gas combustion chamber (CC) is adopted to heat up the airflow to the desired temperature prior to its expansion in the turbine. Such a hybrid solution increases the system flexibility and allows for full-time operation [18]. Furthermore, a recuperator (RP) can be adopted to increase the power cycle efficiency [9]. In the recuperator, the airstream is preheated by the exhaust from the turbine. In this work, the LHTES unit is located downstream of the power cycle in order to exploit the amount of thermal energy contained in the cycle exhaust, with a heat exchanger (HE) connected to a secondary water loop to transfer the recovered heat to the user.

As a result of the selected LHTES subsystem location, the operation of the power cycle is not varied from previous studies on solar-air Brayton cycles were TES devices where disregarded. As a reference solar air Brayton cycle, we select the system presented by De Wet et al. [12]. Such system allows for two power cycle operational modes, namely the *low-temperature receiver mode* and the *high-temperature receiver mode*. The switch between the two operational modes is provided by the use of control valves, which can be used to redirect the air stream according to the operational strategy adopted. When the cycle operates according to *high-temperature receiver* operational mode, the air stream exiting the compressor is heated up in the recuperator prior to its entrance into the solar receiver. On the other hand, concerning the *low-temperature receiver* operational mode, the air stream exiting the compressor is redirected to the solar receiver first and then heated up in the recuperator. As a consequence, the charging conditions of the LHTES unit can vary. Nonetheless, such charging conditions can be directly derived from the conditions of the exhaust of the power cycle and, in this work, the 3.35 $kW_{el}$ power cycle presented in [12] is considered. The LHTES unit is designed to provide heat after the cycle shutdown, i.e. after sunset. The storage unit discharge is thus decoupled from the cycle operation, and it is operated by a dedicated circulation fan. The deriving LHTES operating conditions are summarized in Table 1. In order to limit the system's complexity, air is also adopted as HTF during the unit discharge and the same mass flow rate as per the unit charging is considered.

**Table 1**
Operating conditions considered for the LHTES unit [12].

| *Parameter* | *Value* | *Unit* |
|---|---|---|
| $T_{c,\ LT\text{-}receiver}$ | 747 | K |
| $T_{c,\ HT\text{-}receiver}$ | 547 | K |
| $T_d$ | 293 | K |
| $\dot{m}_{HTF,c}$ | 0.07 | Kg/s |
| $\dot{m}_{HTF,d}$ | 0.07 | Kg/s |
| $T_{amb}$ | 293 | K |

A series of system requirements are defined in order to drive the design decision-making process. A key feature of the thermal system under investigation is its compactness. In particular, the minimization of the distance between the different system components guarantees a reduction in the heat losses from the hot pipes. In this regard, the LHTES unit is envisioned here to be located on the supporting structure of the solar dish. As a consequence, a maximum unit weight of 500 kg is considered. Besides, a relatively low maximum unit cost of 1500 USD is adopted. The cost estimation carried out in this work deals with the material cost value, which is assumed to be dictated by the storage and containment materials selection and thus does not account for the LHTES device manufacturing cost. As a consequence, the cost reported might differ from the final ones. Nonetheless, the estimated costs reported can be confidently used to derive the most cost-effective solution among the PCM-containment pairs under investigation. The design must ensure the unit charge for a charging time below 10 h, i.e. time assumed for the continuous plant operation, considering *low-temperature receiver* operational mode, at the expense of a low-pressure drop (<1 kPa). To ensure a low-pressure drop is crucial to achieving a limited power consumption for the air circulation during the unit discharge process. *In fact, assuming a fan efficiency of 0.4 [19], a fan power consumption value below 200 W is estimated, representing < 6% of the power cycle size.* Finally, given the intended use of the energy system in remote locations, low maintenance and long component durability are desirable. A high component lifespan, above 20 years, is targeted.

### 2.2. Proposed LHTES unit sub-system

The LHTES unit design proposed in this work is based on the TES geometry suggested by Le Roux et al. [9]. A square-helical coil is adopted to deliver and retrieve thermal energy from the storage material domain, as depicted in Fig. 3 (a). The use of the depicted coil geometry allows for ease of manufacturability and for a limited HTF pressure drop [21]. Besides, the use of helical coil heat exchangers in LHTES units has already been successfully demonstrated in the literature [21,22]. A relatively large coil diameter, Ø 88.9x3 mm, was selected and a final surface area of 1.98 $m^2$ was obtained for the heat transfer from or to the pipe walls. The coil design is located in a primary casing which is then filled with the storage material, as shown in Fig. 3(b). The corners of the primary casing were rounded and an inner cavity was added to reduce the PCM volume and meet the weight requirement. In this work, the unit is oriented horizontally, with key dimensions as shown in Fig. 3 (b). At the net of the volume devoted to the coiled tubes, the final primary casing geometry can allow for a 0.073 $m^3$ of PCM. However, only 95% of this volume is considered for the PCM weight estimation, as a 5% volume air gap is accounted at the top of the container to accommodate the materials' expansion. To limit the unit investment cost, Stainless Steel 316L was selected as containment material. Therefore, besides the experimental testing for the thermo-physical properties characterization of the selected storage material candidates, a literature survey was also

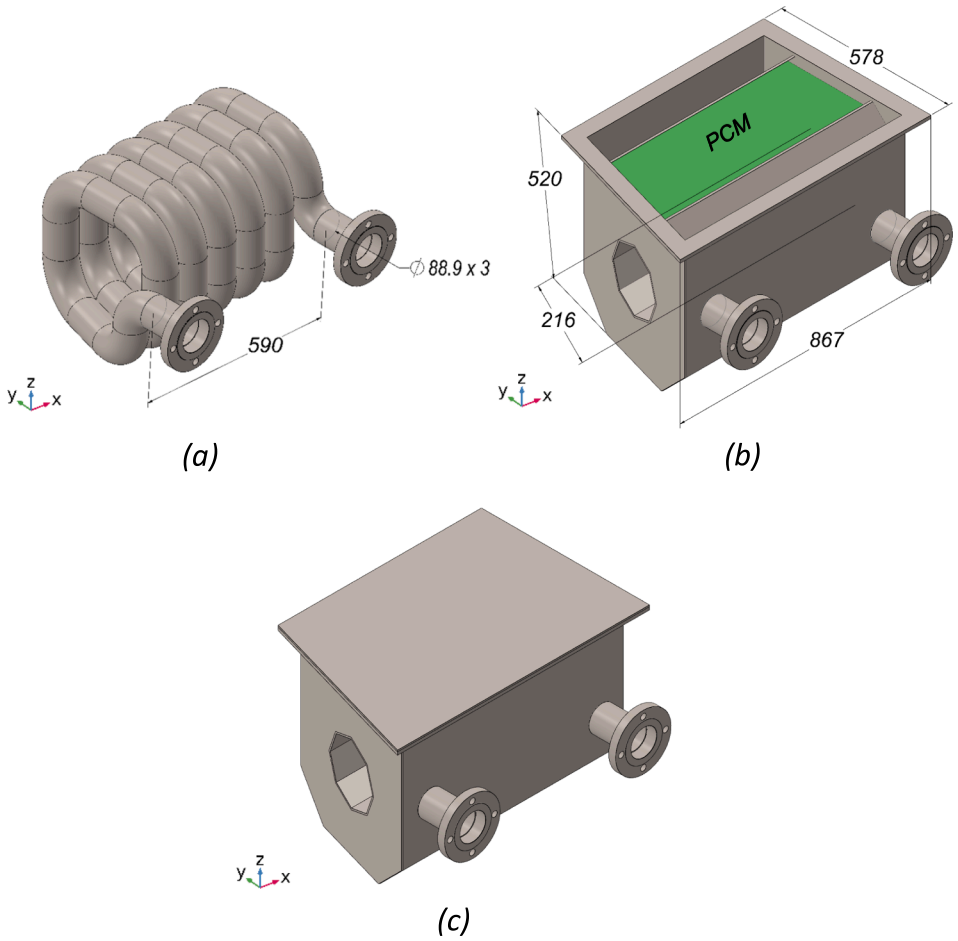


**Fig. 3.** LHTES unit design: (a) square-helical coil; (b) LHTES unit container filled with PCM; (c) LHTES primary casing. The LHTES units' key dimensions are reported in *mm*.

conducted to evaluate the materials' compatibility with Stainless Steel 316L and to estimate the LHTES component lifespan.

## 3. Materials and methods

The steps taken for the end-to-end development of the high-temperature LHTES unit are summarized in Fig. 4. First, the LHTES integration into a small-scale solar air Brayton cycle was analyzed to derive the design requirements and constraints. Thus, such constraints were adopted to select suitable storage and containment materials in the framework of the targeted energy application. Besides, the shortlisted PCMs were characterized through thermo-analytical techniques for the temperature range of operation. A fit-for-purpose LHTES unit geometry was then designed to match the identified system constraints and its performance assessed for each of the shortlisted PCMs by means of a 3D numerical model. In such a way, the most suitable storage material was ultimately selected. Finally, the designed unit was manufactured and tested under realistic operating conditions.

### 3.1. Material selection and characterization

The dual cycle operational mode entails different charging conditions for the LHTES unit. As a consequence, the selection of a PCM with a relatively high melting point, $T_m > 547$ K, would lead to the storage material melting only during the *low-temperature receiver* operational mode, with the LHTES unit working as a sensible storage system otherwise. On the other hand, if a storage material with a lower melting point, $T_m < 547$ K, is selected, lower grade heat storage would be achieved. Two suitable material candidates were therefore selected for each of the aforementioned temperature ranges and the advantages and disadvantages of each material selection are assessed and analyzed throughout the work.

The desired melting point for each operational mode was identified with the aim to maximize the LHTES charging, approximately 700 K for the *low-temperature receiver* operational mode and 500 K for the *high-temperature receiver* operational mode. Two off-the-shelf molten salt candidates were considered from PCM Products Ltd. [23] to limit the material preparation complexity [24], namely the H425 and H230 candidates, while the so-called solar salt candidate (40 $_{wt}$% $KNO_3$ – 60 wt% $NaNO_3$) was considered given its low cost and proven thermal stability along charging and discharging cycles [25]. In addition to molten salts candidates, the use of a pure metallic PCM candidate was preliminarily assessed. Specifically, zinc was identified as the most promising material among the metallic PCM candidates reported by Shamberger et al. [26]. Furthermore, the use of zinc as a storage material was assessed by Zhao et al. [27], highlighting its lower theoretical cost per unit of stored energy compared to state-of-the-art solutions. A summary of the theoretical thermo-physical properties and costs for the shortlisted PCM candidates is reported in Table 2. The reported material costs refer to the South African market, with the solar salt cost estimated from the cost of its raw materials [28,29].

In order to accurately predict the materials' behavior, the shortlisted materials were characterized by thermo-analytical techniques. The materials' latent heat, melting point, and specific heat were obtained through DSC analysis. Sapphire was used as reference material and, given the proven compatibility with all the shortlisted materials,

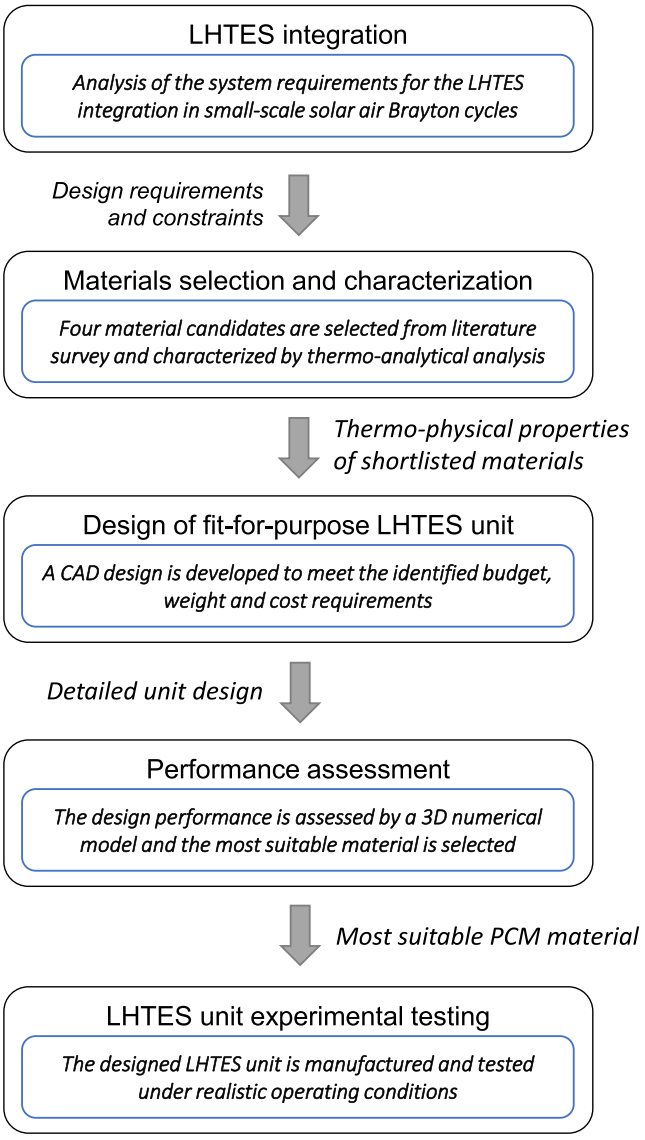


**Fig. 4.** Flow chart summarizes the steps adopted for the end-to-end development of the high-temperature LHTES unit.

aluminum standard holders with a 40 μl volume were selected. The dynamic method adopted for the material testing considered an initial isotherm at ambient temperature, followed by dynamic heating with the heating rate set at 10 K/min. The dynamic heating process ended when the sample temperature reached a temperature approximately 100 K larger than the theoretical melting point, $T_{m,\ th}$. A minimum of three samples were prepared for each material candidate and each sample was subject to two consecutive thermal cycles in a nitrogen environment (100 ml/min). In addition to the DSC analysis, the solar salt thermal diffusivity was measured through LFA analysis. The material sample was placed in an Rd-Rh platinum crucible with 12.5 mm diameter and 2.7 mm height. Again, the tests were performed in a nitrogen environment (100 ml/min) and the thermal diffusivity variation with temperature was calculated over five laser shots.

### 3.2. Numerical model for performance assessment

A 3D numerical model was developed in Comsol Multiphysics v5.6 [32] environment to predict the dynamic performance of the LHTES unit. The influence of the pipes and primary casing thermal masses was considered to be negligible and the computational domain studied in the analysis is presented in Fig. 5, with particular emphasis on the PCM and fluid domains. In the latter, the flow-field is modeled as an isothermal incompressible fluid in steady-state conditions:

$$\begin{cases} \rho_{HTF}\nabla \bullet u = 0 \\ \rho_{HTF}u \bullet \nabla u = \nabla \bullet [-pI + \mu(\nabla u + \nabla \boldsymbol{u}^T)] \end{cases} \tag{3.1}$$

Where $\boldsymbol{u}$ is the velocity field, $p$ is the fluid pressure, $\rho$ is the density, and $\mu$ the dynamic viscosity. The k-ε model is used for the solution of the flow-field equations in the turbulent regime, with the model constants selected from [33]. The stationary flow-field solution is used as an input for the solution of the dynamic heat transfer problem. The heat transfer in the fluid domain is predicted according to:

$$\rho_{HTF}c_{p,HTF}\frac{\partial \mathrm{T}}{\partial t} + \rho_{HTF}c_{p,HTF}\boldsymbol{u}\,\nabla T_{HTF} - k_{HTF}\nabla \mathrm{T} = 0 \tag{3.2}$$

Where $T$ is the temperature, $c_p$ is the specific heat, and $k$ is the thermal conductivity. Concerning the PCM region, the effect of natural convection is assumed to be negligible [34], and the enthalpy-porosity method is used to solve the phase-change problem:

$$\frac{\partial}{\partial t}(\rho_{PCM}h) = \nabla \hat{\mathrm{A}}\cdot(k_{PCM}\nabla \mathrm{T}) \tag{3.3}$$

Where the specific enthalpy, $h$, is a sum of the sensible enthalpy and the latent heat of the PCM, $L$:

$$h = h_{ref} + \int_{T_{ref}}^{T} c_{p,PCM}d\mathrm{T} + fL \tag{3.4}$$

Note that $f$ represents the liquid fraction, used to track the amount of liquid PCM. The HTF adopted in the energy system corresponds to air, which was assumed to behave as an ideal gas [35]. For the solution of equation (3.1), the HTF properties were taken at the average temperature value between the initial and the charging conditions. As a consequence, the flow-field solution varies with the considered power cycle operational mode.

The behavior of the LHTES unit was predicted for a consecutive charging and discharging process, i.e. for a full cycle. In particular, a 10 h charge followed by a 5 h discharge was considered in the numerical simulations. The inlet temperature was ramped up from the ambient temperature value to the charging condition in a 5 min time. This ensures an at-equilibrium system at the initial time, leading to a larger convergence speed of the time-dependent problem [36]. For the same reason, the transition between charging and discharging conditions was considered to take place in 10 min. The dynamic HTF inlet temperature profile was imposed at the fluid inlet interface, while null heat flux conditions were assumed at the fluid outlet interface. A Robin boundary condition type was used to model the heat losses towards the environment, with the global heat transfer coefficient, $h_{global}$, calculated as a series of two thermal resistances: a conductive thermal resistance considering the insulation material, specifically 0.1 m of fiberboard F-

**Table 2**
Summary of the theoretical thermos-physical properties and estimated costs for the shortlisted PCM candidates.

| PCM | $T_{m,th}$ [K] | $L_{th}$ [kJ/kg] | $c_{p,s,th}$ [kJ/kg] | $\rho_s$ [kg/m$^3$] | $\rho_l$ [kg/m$^3$] | Cost per kg [$/kg] | Cost per kWh [$/kWh] |
|---|---|---|---|---|---|---|---|
| H425 [24] | 698 | 220 | 1.6 | 2100 | 2100 | 10.3 | 42.0 |
| Zinc [27,30] | 692 | 112 | 0.4 | 7140 | 6510 | 2.9 | 37.6 |
| H230 [24] | 503 | 105 | 1.5 | 1553 | 1553 | 12.2 | 60.5 |
| Solar salt [25,31] | 495 | 100 | 1.5 | 2200 | 1900 | 1.0 | 5.0 |

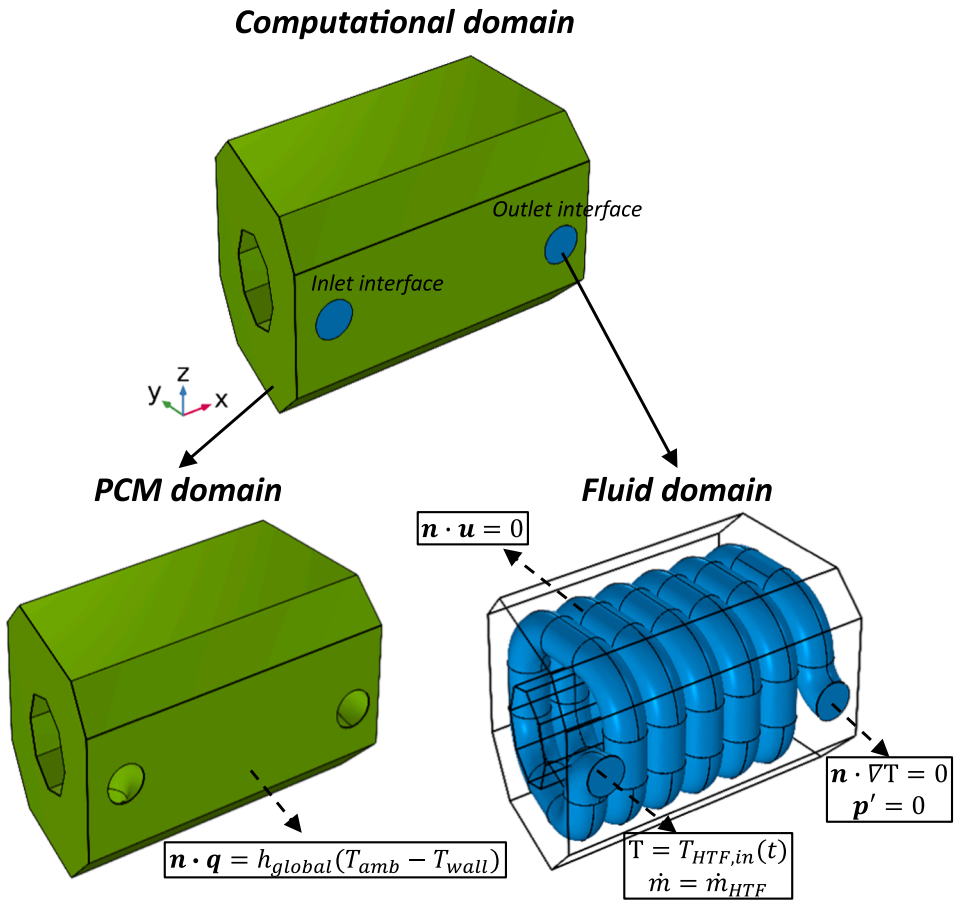


**Fig. 5.** Computational domain and boundary conditions.

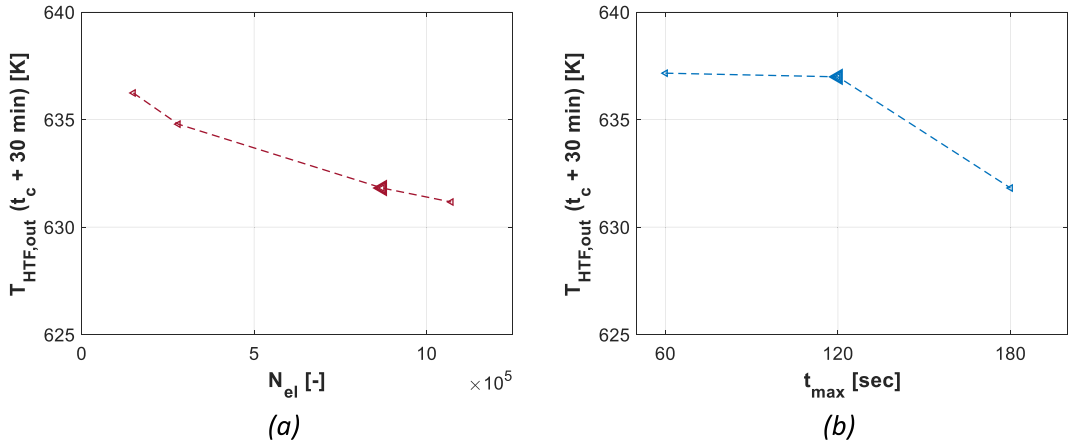


**Fig. 6.** xxx.

1260 SB [37], and a convective thermal resistance. The same flow direction is considered in both charging and discharging processes, and a fully developed flow with a mass flow rate of 0.07 kg/s is imposed at the fluid inlet interface. Both PCM and fluid domains were assumed at ambient temperature at the initial time, t = 0.

Fig. 6 convergence studies **for the HTF outlet temperature at time t = tc + 30 min**: (a) mesh convergence study; (b) maximum time-step convergence study.An unstructured tetrahedral mesh with 871 000 elements is adopted in the analysis. The number of elements was selected after a mesh convergence study, where a 0.18% discrepancy was measured for the HTF outlet temperature compared to a 1 071 000 elements tetrahedral mesh, as reported in Table 4. A second-order BDF scheme is adopted for the time-dependent study solution, with a time-step adaptation scheme considering a maximum time-step selected at

**Table 3**
LHTES unit weight and investment cost for each of the shortlisted PCMs.

| | *H230* | *Zinc* | *H425* | *Solar Salt* |
|---|---|---|---|---|
| $m_{PCM}$ [kg] | 113.4 | 475.2 | 153.3 | 138.6 |
| $m_{LHTES}$ [kg] | 278.6 | 640.4 | 318.5 | 303.5 |
| Cost [USD] | 1739.5 | 1746.3 | 1989.4 | 618.2 |

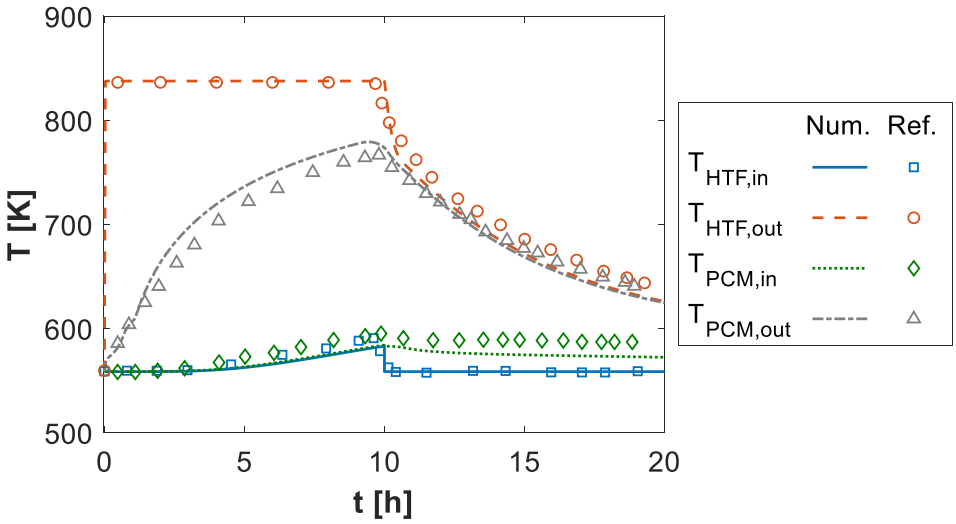


**Fig. 7.** Model validation against the data reported by Tehrani et al. [34]. The notations $T_{PCM,\ in}$ and $T_{PCM,\ out}$ refer to the local PCM temperature in proximity of the HTF inlet and outlet interfaces, respectively.

120 s. Besides, an initial time-step of 0.1 s is imposed to ensure a smooth convergence rate during the initial stages of the numerical analysis. The numerical model is validated against the data presented by Tehrani et al. [34]. Here, the authors investigated the dynamic operation of a shell-and-tube LHTES unit operated with lead as PCM. A maximum discrepancy below 5% is measured between the predictions obtained from the numerical model presented in this section and the reference data, concluding that the developed numerical framework can be confidentially adopted to predict the LHTES unit dynamic performance.

### 3.3. LHTES unit manufacturing and experimental setup

The LHTES unit was manufactured in the heavy machinery laboratories at the University of Pretoria. The square helical coil was constructed from the welding of small sections of straight pipes and elbows, while the primary casing was laser cut from 3 mm thickness stainless steel 316L plates. The primary casing was welded to the coil in order to avoid PCM leakages in the proximity of the coil ends. Fig. 7 presents the experimental setup adopted for the unit testing. The unit testing was performed at the University of Pretoria, with the experimental campaign location and adopted components depicted in Fig. 2. Nonetheless, for the LHTES subsystem testing, the solar receiver and recuperator components were not employed. The storage component was connected to the combustion chamber, in a way that a nearly constant charging temperature could be provided. The unit discharge was instead operated at ambient temperature by the by-pass of the combustion chamber component. The LHTES unit testing was conceived to replicate the *high-temperature receiver* operational mode conditions reported in Table 1. The desired charging temperature was obtained through the manual regulation of the gas flow in the combustion chamber, while a constant mass flow rate (0.07 kg/s) was ensured by means of a dedicated petrol blower and a SUTO S421 mass flow meter. Flexible steel hoses were adopted for the components connection and thermal resistant paste was added to reduce heat losses. The charging process testing was considered complete at stationary conditions, i.e. for nearly constant temperature measurements, while the discharging process was ended when HTF outlet temperature of 373 K was recorded. The amount of energy stored in the unit was estimated by assuming the LHTES unit temperature as the average temperature of the measured values, while the amount of energy transfer to the HTF can be directly derived from the HTF temperature drop. The difference between the two energy fluxes is assumed as heat losses.

Thermocouples were located along the coil length in order to monitor the PCM temperature variation at different turns of the coil. TC50 Surface Thermocouples were purchased from Wika Instruments [38], which guarantees high durability against corrosion from the solar

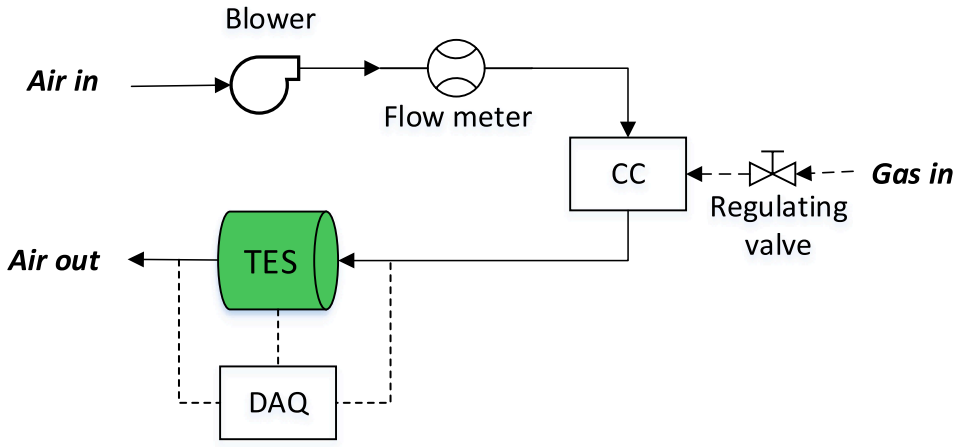


**Fig. 8.** Experimental setup for the LHTES unit testing in realistic operating conditions. A regulating valve is adopted to adjust the amount of gas entering the combustion chamber to maintain a desired inlet temperature in the LHTES sub-system.

**Table 4**
DSC measurement results and estimated errors for the melting, l → s, and solidification, s → l, of the shortlisted PCMs.

| | *Solar salt* | *H230* | *H425* | *Zinc* |
|---|---|---|---|---|
| $T_{l\to s}$ [K] | 496.00 ± 0.12 | 506.18 ± 1.71 | 701.37 ± 0.77 | 696.20 ± 0.62 |
| $L_{l\to s}$ [kJ/kg] | 108.52 ± 1.98 | 103.66 ± 2.52 | 224.17 ± 4.11 | 105.50 ± 1.16 |
| $T_{s\to l}$ [K] | 492.99 ± 0.5 | 494.94 ± 1.36 | 690.86 ± 0.96 | 687.18 ± 0.3 |
| $L_{s\to l}$ [kJ/kg] | 112.12 ± 1.73 | 99.85 ± 1.82 | 184.98 ± 4.39 | 105.90 ± 1.08 |

salt material. The thermocouples were welded onto the coil to ensure reliable temperature monitoring of the coil surface, with the locations of the thermocouples presented in Fig. 8 (a). A total of six thermocouples, i.e. one for each turn of the coil, are adopted. Besides, five thermocouple probes are used to monitor the PCM bulk temperature variation near the primary casing inner cavity. The thermocouple probes are placed through the gaps between coil turns, as can be appreciated in Fig. 8 (b). Finally, two additional thermocouples are installed at the coil inlet and outlet.

## 4. Results and discussion

The storage material quantities and estimated investment costs are listed in Table 3 for each of the shortlisted material candidates. While the zinc, H425, and H230 solutions would lead to a small difference in investment cost, a significant reduction is achieved by the use of solar salt as storage material. Such cost reduction is dictated by the low cost of the PCM constituents, i.e. $KNO_3$ and $NaNO_3$. Besides, despite the reduced primary casing volume, the use of zinc still presents a final mass above the targeted threshold. That is, despite their attractive thermophysical properties, the selection of metallic PCMs in weight-constrained LHTES applications results to be not suitable. On the other hand, the weight constraint is satisfied by the use of the molten salt candidates.

### 4.1. Material characterization results

The DSC results for a single material sample of each of the shortlisted PCMs are shown in Fig. 9. Here, the heat flow provided to the sample is reported as a function of temperature, and heat flow peaks are measured in correspondence with the sample melting or solidification. Overall, during the sample's heating process, corresponding to negative heat fluxes, such peaks are measured at larger temperature values compared to the sample cooling. That is, sub-cooling is consistently measured regardless of the investigated material candidate. While milder discrepancies are observed in the instances of zinc and solar salts, peak differences up to 11.2 K and 12.9 K are measured for the commercial molten salts, H425 and H230 respectively. Although sub-cooling could be mitigated by the addition of appropriate nucleating agents [39], the measured phase transition temperature reduction does not constitute a major limitation for the targeted energy application. Besides, Tay et al. [40] observed the sub-cooling effect to be more unlikely to occur in the case of large PCM bulks. The measured melting and solidification temperatures, along with the latent heat, are summarized in Table 4. Here, the reported absolute errors refer to the standard deviation value measured over the three material samples. Overall, good agreement is measured between the different samples, with a maximum relative error of below 2%. Besides, a low discrepancy with the theoretical values reported in Table 2 is measured (below 7.1%).

The solar salt thermal conductivity was measured by LFA analysis in the temperature range from 523 K to 773 K. A small variation with temperature was found (<5%), thus a constant thermal conductivity of 0.52 W/m/K can be assumed for the intended application. Concerning zinc, Powell [30] reported a sharp reduction ( ≈ 43%) between the solid and liquid thermal conductivity. Finally, Table 5 Thermo-physical properties collected during the storage material characterization. The materials' melting temperature, $T_m$, is considered as the average value between the measured $T_{l\to s}$ and $T_{s\to l}$ values. While the melting range, $\Delta T_m$, is averaged from the onset and endset points of the raw measured peaks for the heating process.

The suitability of each of the shortlisted materials to be operated at the maximum envisioned working temperature is evaluated by heating up small material quantities to a temperature of 750 K. No significant mass deterioration was observed for the zinc, H425, and the solar salt candidates. However, full material volatilization of the H230 candidate was measured, thus precluding its use in the targeted energy system. The estimated component lifespan for the LHTES unit operated with the shortlisted PCMs is reported in Table 6. Given its poor compatibility with stainless steel, a short component lifespan is estimated for zinc, which significantly penalizes its use as suitable storage material. Two alternative containment material options were also assessed: (i) the use of ultra-low silicon steel as containment material (ARMCO) [41], and (ii) the use of Wc/CO HVOF-thermal spray coatings to limit the molten

**Table 5**
LHTES unit weight and investment cost for each of the shortlisted PCMs.

| | *H230* | *Zinc* | *H425* | *Solar Salt* |
|---|---|---|---|---|
| $m_{PCM}$ [kg] | 113.4 | 475.2 | 153.3 | 138.6 |
| $m_{LHTES}$ [kg] | 278.6 | 640.4 | 318.5 | 303.5 |
| Cost [USD] | 1739.5 | 1746.3 | 1989.4 | 618.2 |

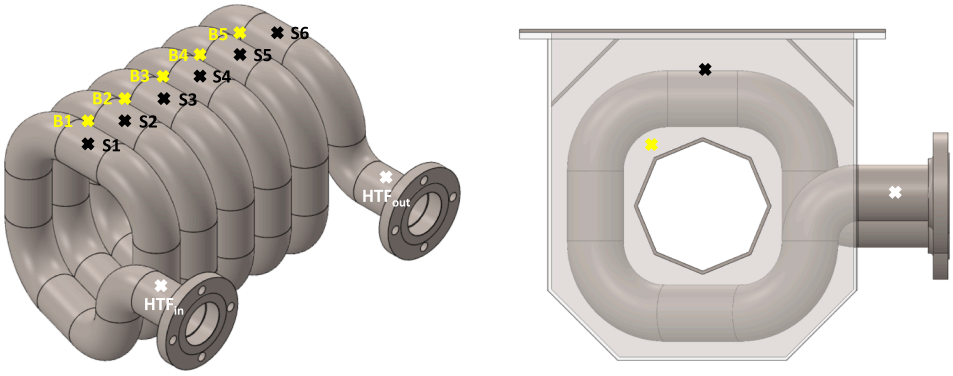


**Fig. 9.** Thermocouple locations: (a) isometric view of the coil with thermocouple probes and weld-on thermocouples; (b) side view of the coil with detail on the location of the weld-on thermocouples and thermocouple probes.

**Table 6**
DSC measurement results and estimated errors for the melting, l→s, and solidification, s→l, of the shortlisted PCMs.

| | *Solar salt* | *H230* | *H425* | *Zinc* |
|---|---|---|---|---|
| $T_{l\to s}$ [K] | 496.00 ± 0.12 | 506.18 ± 1.71 | 701.37 ± 0.77 | 696.20 ± 0.62 |
| $L_{l\to s}$ [kJ/kg] | 108.52 ± 1.98 | 103.66 ± 2.52 | 224.17 ± 4.11 | 105.50 ± 1.16 |
| $T_{s\to l}$ [K] | 492.99 ± 0.5 | 494.94 ± 1.36 | 690.86 ± 0.96 | 687.18 ± 0.3 |
| $L_{s\to l}$ [kJ/kg] | 112.12 ± 1.73 | 99.85 ± 1.82 | 184.98 ± 4.39 | 105.90 ± 1.08 |

**Table 7**
Thermo-physical properties collected during the storage material characterization.

| | *H230* | *Solar Salt* | *H425* | *Zinc* |
|---|---|---|---|---|
| $T_m$ [K] | 500.6 | 494.5 | 696.1 | 691.7 |
| $L$ [kJ/kg] | 101.8 | 110.8 | 204.6 | 105.7 |
| $\Delta T_m$ [k] | 6.5 | 14.3 | 7.5 | 5.5 |
| $c_{p,s}$ [kJ/kg] | 1.2 | 1.4 | 1.5 [23] | 0.4 [30] |
| $c_{p,l}$ [kJ/kg] | 1.2 | 1.4 | 1.5 [23] | 0.4 [30] |
| $k_s$ [W/m/K] | 0.50 [23] | 0.52 | 0.57 [23] | 116.0 [30] |
| $k_l$ [W/m/K] | 0.50 [23] | 0.52 | 0.57 [23] | 50.0 [30] |

zinc attacks on stainless steel 316L [42]. However, despite reduced corrosion rates, none of the investigated containment solutions for zinc led to estimated component lifespans above 1 year.(SeeTable 7.).

### 4.2. Numerical results

#### 4.2.1. Fluid dynamics performance

The predicted pressure contours in the coil are shown in Fig. 10. For both operational modes, larger localized pressure variations are visible at the two ends of the unit due to the higher coil curvature. As expected, an increase of pressure is predicted near the outer wall of the coil bends, while a reduction of pressure is predicted near the inner walls. As a consequence, larger local velocities are present on the outer side of the coil, while lower local velocities are observed on the inner side. Overall, given the increase of the air dynamic viscosity with temperature, larger pressure variations are predicted in the case of larger $T_{HTF}$. In fact, regarding the unit's global performance, a 1.07 kPa pressure drop is predicted in the case of the *low-temperature receiver* operational mode, which reduces to 1.0 kPa in the case of the *high-temperature receiver* operational mode. That is, the pressure drop constraint identified in section 2 is exceeded by 7% during the former operational mode. Nonetheless, this excess is considered to be acceptable in the scope of the system operation, although a by-passing system is recommended to limit the cycle pressure drop in case of a fully-charged TES.

#### 4.2.2. Thermal performance

The LHTES unit's thermal performance is evaluated in this section considering the unit operation with zinc, H425 and the solar salt candidates. The numerical framework adopted for the performance comparison is fed with the materials' thermo-physical properties collected during the material characterization step. Besides, for material properties varying with the material phase, a linear correlation with the local liquid fraction, *f*, is assumed. Fig. 11 (a) shows the predicted state of charge, SOC, and liquid fraction evolutions in time in the instance of the *low-temperature receiver* operational mode. Thanks to its large material

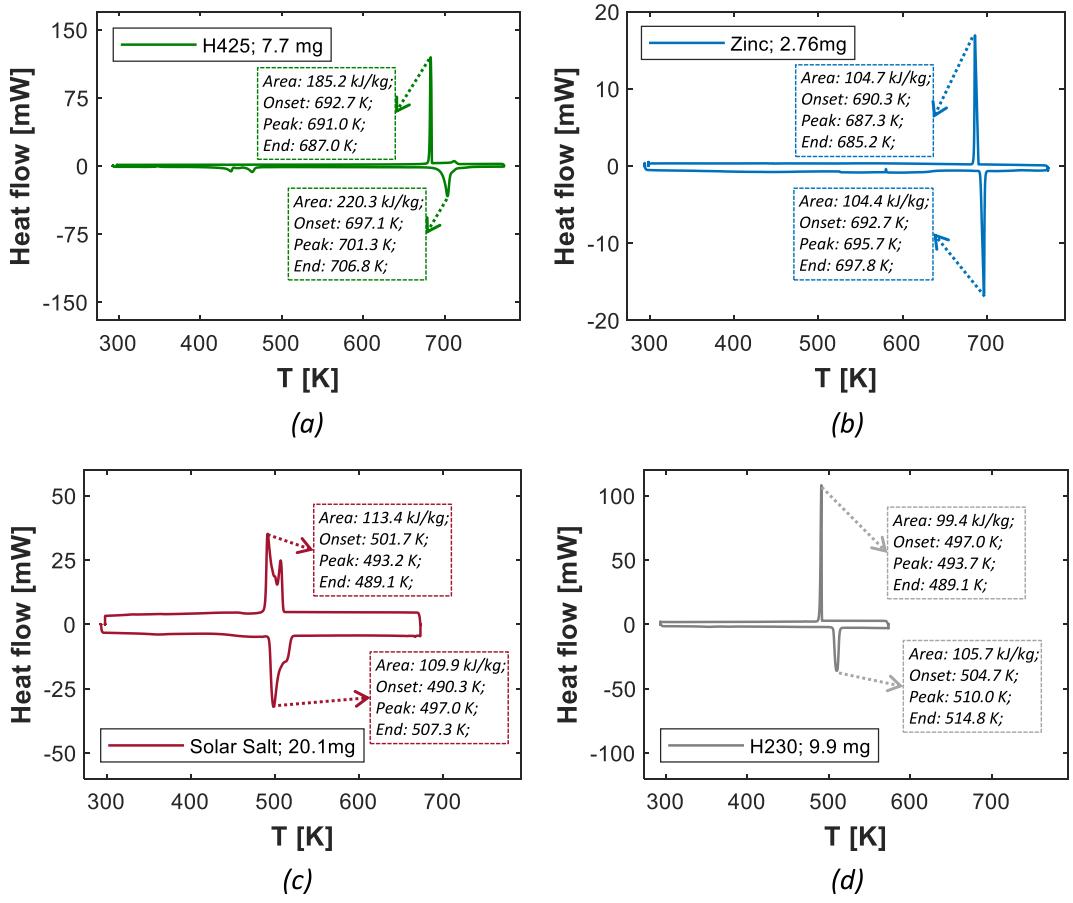


**Fig. 10.** DSC analysis results for a single material sample for each of the shortlisted PCMs: (a) H425; (b) Zinc; (c) Solar Salt; (d) H230.

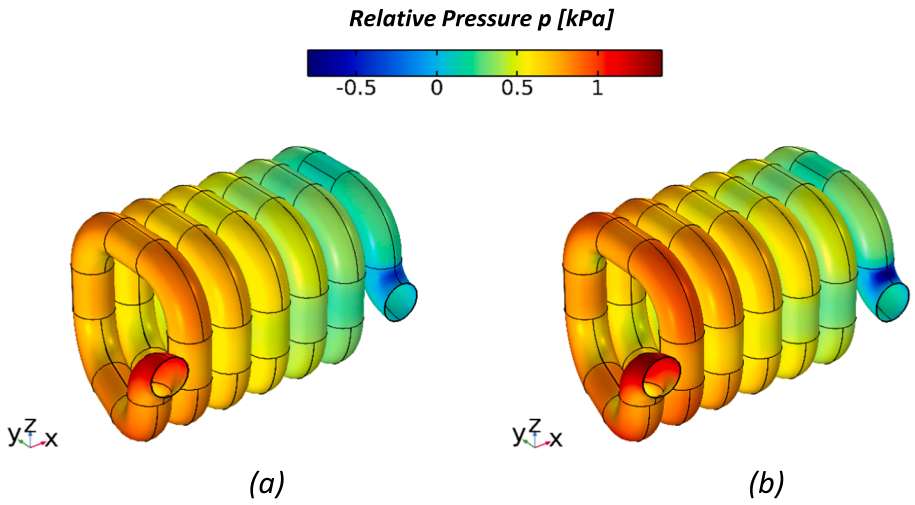


**Fig. 11.** Pressure contours for (a) *high-temperature receiver* operational mode and (b) *low-temperature receiver* operational mode.

thermal conductivity, the shortest charging time is achieved for zinc, while the H425 candidate shows a charging time above the selected threshold ($t_{c,\ 90\%,\ H425} > 10$ h). That is, the poor heat transfer performance of H425 precludes its use in the targeted energy system. The SOC evolution in time for zinc shows a change of steepness after ≈ 1h, i.e. for SOC values ≈50%. Such a change of steepness coincides with the beginning of the PCM melting. In fact, the PCM melting provides additional thermal inertia to the charging process, ultimately reducing the rate of the SOC increase. The same trend is not evident for the unit's operation with the solar salt due to the larger temperature difference between the charging temperature and the material melting point. Regardless of the storage material candidate, no symmetric behavior is predicted between the charging and discharging histories. In fact, the LHTES unit's discharge rates resulted to be higher than the charging rates. Such behavior can be directly attributed to the large temperature difference between discharge temperature and melting points in the instances of zinc and H425. However, a lower temperature difference is present for what concerns solar salt. Here, the higher discharge rates can be attributed to (i) the incomplete LHTES charging, (ii) the favorable temperature distribution after the charging process, and (iii) the heat loss 'contribution' to the discharging process. In particular, points (i) and (ii) are predicted to play a crucial role in the unit's discharging rate. The incomplete charging of the LHTES unit entails the PCM regions away from the coil walls to present a poor local SOC-value. Thus, when the discharge process takes place, the PCM regions to be discharged are the ones near the coil walls, where heat transfer is stronger.

Fig. 11 (b) exhibits the state of charge and liquid fraction evolution in time in the instance of the *high-temperature receiver* operational mode. Here, the maximum state of charge, $SOC_{HTreceiver,max}$, is defined by considering the LHTES unit with a final homogeneous temperature equal to $T_{c,\ HT\ receiver}$. However, such a maximum state of charge cannot be achieved in the instance of zinc and H425, as these candidates present a melting point below the investigated charging conditions. Concerning the solar salt candidate, the liquid fraction evolution in time is predicted to progress at a lower rate compared to the *low-temperature receiver* operational mode, as a consequence of the lower temperature drivers

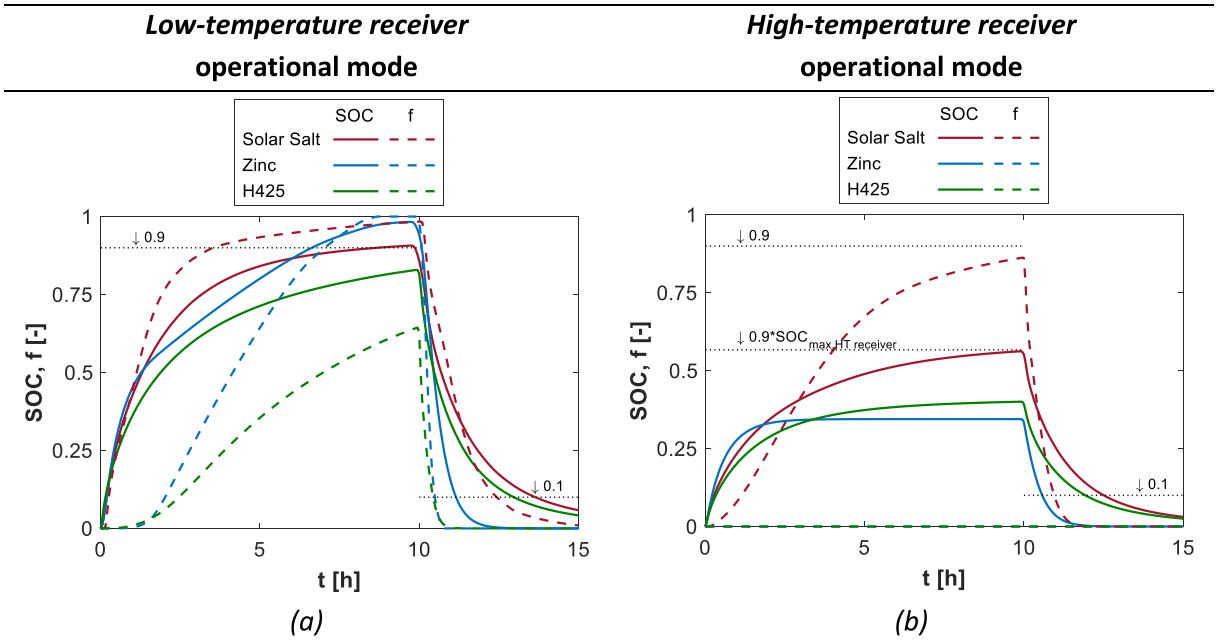


**Fig. 12.** State of charge, SOC, and liquid fraction, *f*, evolution in time for the shortlisted PCM candidates for (a) *low-temperature receiver* operational mode and (b) *high-temperature receiver* operational mode.

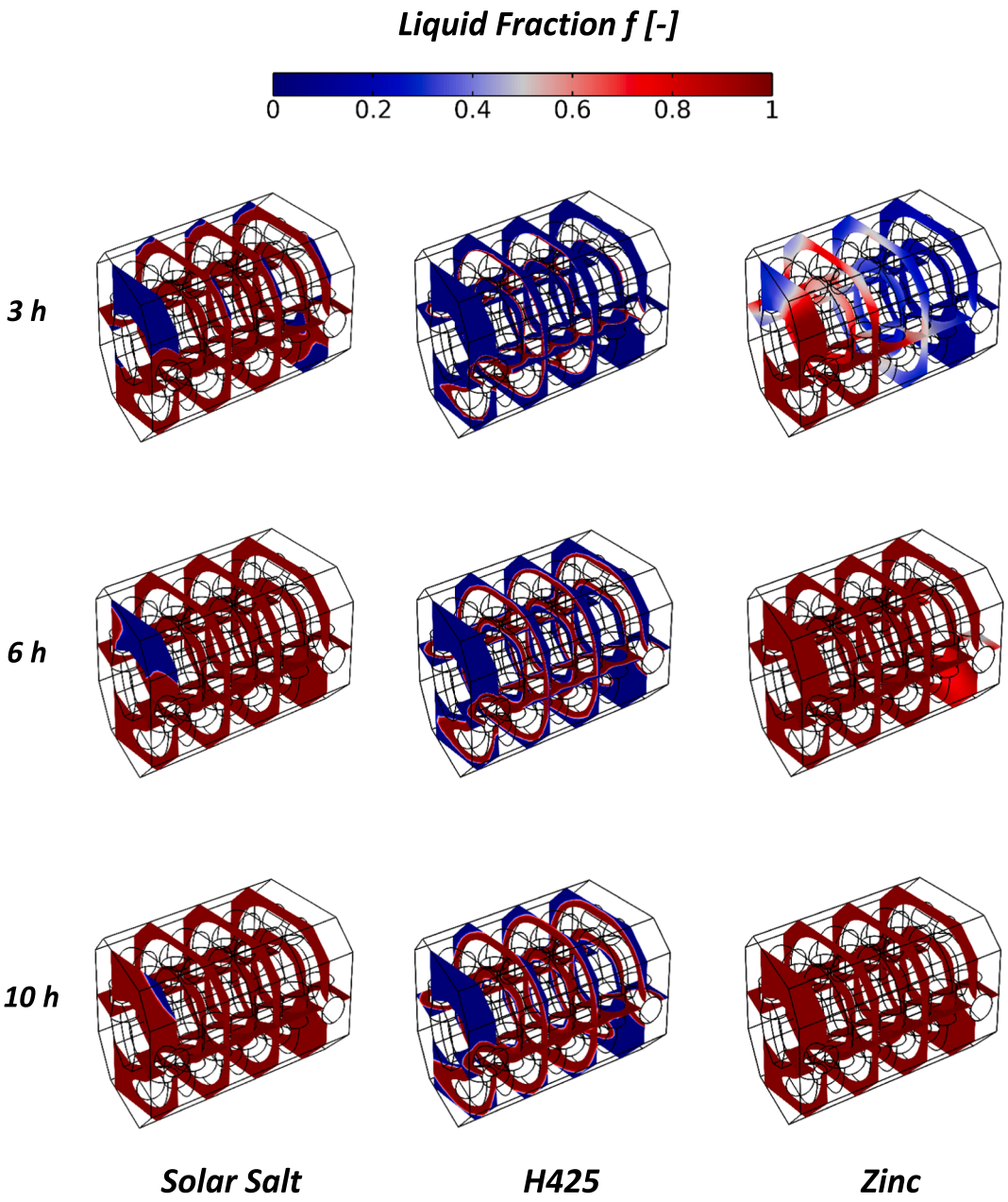


**Fig. 13.** Liquid fraction contours evolution in time for the charging process in *low-temperature receiver* operational mode with solar salt, H425 and zinc.

involved. Nonetheless, very close proximity (-0.007) is predicted between the targeted $0.9 \bullet SOC_{HTreceiver,max}$ value and the predicted SOC after 10 h charging time, demonstrating satisfactory LHTES unit charging performance also during continuous *high-temperature receiver* operational mode.

Fig. 12 presents the liquid fraction contours evolution in time for the LHTES unit operated with the three shortlisted PCM candidates in the instance of *low-temperature receiver* operational mode. Regardless of the material candidates, the melting front propagates from the HTF walls towards the primary casing boundaries, and a negligible influence of the heat losses towards the environment is observed due to the large insulation thickness. As a consequence of the low material thermal conductivity, and thus of the low-temperature gradients in the PCM domain, a sharp melting front is predicted for the molten salt candidates. On the other hand, less sharp melting fronts are observed for zinc as the temperature gradient in the PCM region results to be less pronounced. Besides, for short charging times, e.g. t = 3 h, PCM regions with full melting are present near the HTF inlet (on the left), while poor material utilization is present near the HTF outlet (on the right). Again, this liquid fraction inhomogeneity derives from the good thermal properties of metallic PCMs. In fact, the good heat transfer rate between the PCM regions and the HTF entails an HTF temperature reduction along with the coil. Concerning the molten salts candidates, the melting front appears to propagate radially from the coil walls, i.e. on the xy-planes, towards the external primary casing boundaries, with limited variations predicted along the coil axial direction, i.e. x-direction. As a consequence of the reduced local velocity, the PCMs regions in proximity of the outer side of the coil bends present a low melting rate. Nonetheless, such an effect is found to have a limited influence on the overall thermal performance. Besides, the PCM regions between the coil and the inner cavity result to be fully melted after a 10 h charging regardless of the considered storage material. That is, a reduced inner cavity volume could be considered in order to increase the storage unit size. Regardless of the analyzed material, under-utilized material regions are present at the two ends of the primary casing, i.e. in the proximity of the coil inlet and outlet interfaces. One way to mitigate the

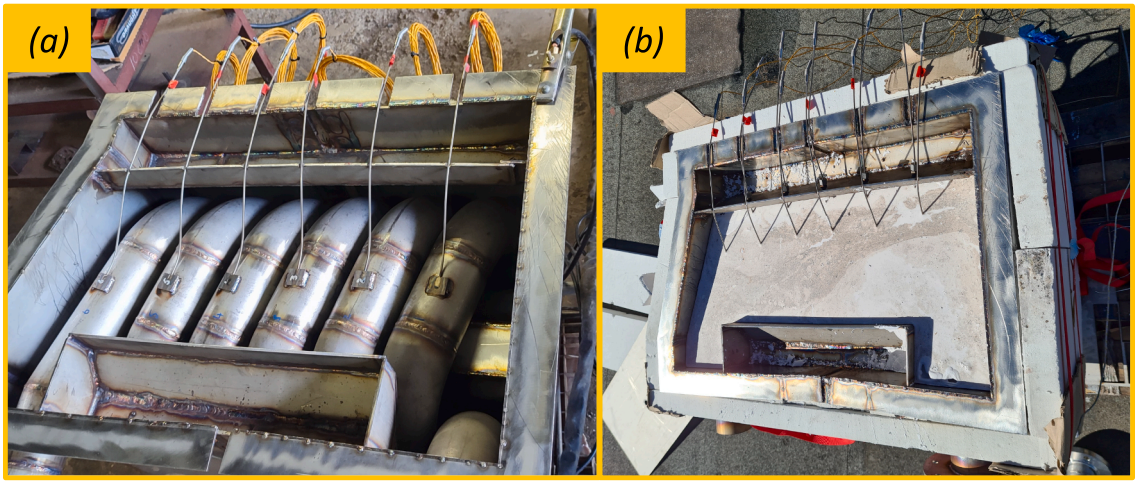


**Fig. 14.** LHTES unit manufacturing: (a) coil, primary casing, baffles, and thermocouples; (b) LHTES unit filled with 151 kg of solar salt.

impact of the coil ends on the poor local material utilization is to lift the inlet and outlet interfaces along the z-axis to reduce the maximum distance between the PCM and HTF wall.

### 4.3. Experimental performance results

In agreement with the material characterization and numerical results, the solar salt (40 $_{wt}$% $KNO_3$ – 60 wt% $NaNO_3$) candidate is identified as the only PCM candidate to meet the system requirements and is thus selected as the most suitable storage material. Hence, a sufficient amount of storage material was prepared to test the performance of the proposed LHTES unit. The solar salt was prepared in batches of approximately 15 kg each. Each batch was heated up by means of a Sievert torch until the complete melting of the mixture. Thus, the melted PCM was filled in the LHTES primary casing. However, during the coil manufacturing process, the heat-induced distortion caused the coil pitch to increase, leading to a final pitch value that was hard to accurately measure. To ensure a sufficient pipe-to-casing fit for welding, the primary casing length was increased by an additional 30 mm (x-direction). As a consequence, an additional 18 kg mass of solar salt was needed to ensure the unit coil be fully immersed in the liquid PCM. That is, a final solar salt mass of 151 kg was adopted in the manufactured unit, leading to a maximum theoretical stored energy of 20.0 kWh. Fig. 13 (b) presents the LHTES unit filled with 151 kg of solar salt in the solid state.

The temperature measurements recorded during the LHTES unit testing are reported in Fig. 14. A nearly constant HTF inlet temperature during the charging process is obtained by the regulation of the gas flow in the combustion chamber, with maximum variations of –33 K compared to the desired $T_{c,\ HT\ receiver}$ value at time 1.1 h. Regardless of the thermocouple location, the temperature gradients reduce when the local temperature approximates the material melting point. Nonetheless, a sharp temperature variations are measured in the PCM bulk measurements when the local temperature reaches the melting point, e.g. at 4.1 h for B1 and 5.8 h for B4. The authors attribute these sharp variations to solid PCM falling in the lower part of the primary casing and thus to liquid material raising to the thermocouple level. Given the fact that gravity effects are neglected in the numerical model, such temperature variations were not observed in the numerical predictions. Nevertheless, the comparison of the energy balances reported in Table 9 exhibits a satisfactory agreement between the experimental and numerical amount of energy stored in the PCM, $E_{PCM}$. As a consequence, the approximation to null gravity effects was found to be acceptable in the scope of the current investigation.(SeeFig. 15.Table 10.).

For similar thermocouple locations along the coil axial length, the measured bulk temperature result is lower than the surface temperatures due to the heat transfer resistance in the storage material. A relatively large temperature difference is measured between B4 and B5 as a consequence of the end effect at the coil outlet. Nonetheless, regardless of the thermocouple location, stationary conditions are achieved during the charging process at approximately 525 K. Thermocouple S6 is the last to reach such stationary conditions, at time t ≈ 9.1 h. That is, for the LHTES unit charging in *high-temperature receiver* operational mode, charging times above 9 h are not beneficial to the unit state of charge.

**Table 8**
Estimated lifespan for the LHTES component operated with the shortlisted PCM candidates; the reported corrosion rates refer to a temperature of ≈750 K.

| | *H425* | *Zinc* | *H230* | *Solar salt* |
|---|---|---|---|---|
| *Δm [mg/cm²/h]* | – | 3.0 [42] | – | 2.6E-3 [45] |
| *H [mm/year]* | – | 5.58 | – | 4.74E-03 |
| *Lifespan [years]* | > 5 [23] | ≈ 0.2 | ≈ 0.0 [(a)] | > 20 |

[(a)] H230 maximum temperature of operation was measured below the envisioned charging temperature for the *low-temperature receiver* operational mode.

**Table 9**
Estimated pressure drop by CFD analysis considering *low-temperature receiver* and *high-temperature receiver* operational modes.

| | *HT receiver Operational mode* | *LT receiver Operational mode* |
|---|---|---|
| Δp [kPa] | 1.00 | 1.07 |

The energy balances calculated from both the numerical and experimental frameworks are reported in Table 8. Despite the 18 kg difference in storage mass, a good agreement in the amount of energy stored is calculated. However, the experimental results show a 35.1 kWh energy retrieved from the HTF, thus 15.4 kWh larger than in the numerical framework. Such discrepancy can be attributed to the conservative heat losses assumed in section 3.2. In particular, the use of a thermal camera highlighted large local heat losses near the coil ends and for the unit topside, where the thermocouple insertions made it more difficult to insulate the unit properly. The efficiency of the waste heat recovery, ε, is quantified here as the ratio between the amount of energy transferred to the HTF during the discharging process, $E_{HTF,d}$, over the amount of energy retrieved by the HTF during the charging process, $E_{HTF,c}$:

$$\varepsilon = \frac{E_{HTF,d}}{E_{HTF,c}} \tag{4.1}$$

Regarding the measured performance, a relatively high heat

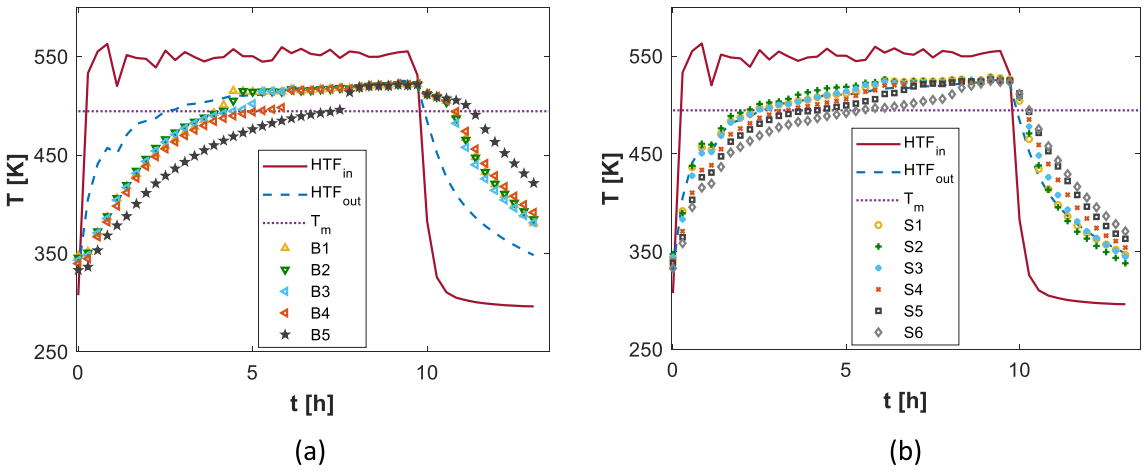


**Fig. 15.** HTF and PCM local temperatures evolution in time from the LHTES unit experimental testing: (a) immersed thermocouples and (b) weld-on thermocouples.

**Table 10**
Energy balances after a 10 h charging process in *high-temperature receiver* operational mode followed by 3.3 h of discharging process for the numerical and experimental results.

| | *Charging* | | *Discharging* | |
|---|---|---|---|---|
| | *Exp.* | *Num.* | *Exp.* | *Num.* |
| $E_{PCM}$ [kWh] | 17.3 | 17.1 | 12.8 | 14.1 |
| $E_{HTF}$ [kWh] | 35.3 | 18.9 | 21.1 | 15.0 |
| $E_{losses}$ [kWh] | 18.0 | 1.8 | 8.3 | 0.9 |

recovery efficiency is calculated, ε=0.60. Again, due to the underestimation of the heat losses towards the environment, a higher heat recovery efficiency was predicted by means of the numerical model (up to 0.79). As a comparison, Johar et al. [43] measured an efficiency of 0.38 in the instance of an LHTES device designed for the recovery of engine exhausts, while Ortega-Fernández et al. [44] predicted an efficiency value around 0.65 in the context of the steelwork industry.

## 5. Conclusions

In this work, the design and testing of a high-temperature LHTES unit integrated into small-scale solar air Brayton cycles are presented. For the first time, the storage sub-unit is located downstream of the power cycle and used to serve heating applications after sunset. The selection of the most suitable storage material was carried out by the definition of a series of cost, durability, performance, and compactness constraints and through the use of a combination of experimental and numerical methods. Thus, the proposed LHTES unit was filled with the identified most suitable PCM and operated under realistic operating conditions. From the end-to-end development of the high-temperature LHTES subsystem, the following key conclusions can be derived:

- The huge potential for waste heat recovery in solar-air Brayton cycles can be exploited by means of LHTES technologies. However, the variable charging conditions deriving from the dual cycle operational modes lead to a non-trivial storage material selection. In agreement with the identified temperature ranges of operation, four storage material candidates were selected consisting of one pure metal and three molten salts.
- The most suitable storage material selection process resulted to be driven by design aspects that are typically overlooked in the literature. In particular, despite the superior thermal properties owned by the investigated metallic PCM candidate, i.e. zinc, this was found to be incompatible with commercial containment materials, thus requiring expensive solutions to achieve satisfactory component lifespans. Besides, the need for light storage unit solutions favored the use of molten salt candidates.
- The so-called solar salt was identified as the most suitable PCM for the targeted energy system. The conducted numerical predictions showed a final state of charge in close proximity to the theoretical maximum values in the instances of both investigated power cycle operating modes. That is, the proposed LHTES subsystem operated with solar salt can achieve a satisfactory state of charge regardless of the adopted power cycle operational strategy.
- The proposed LHTES unit configuration filled with 151 kg of solar salt was tested under realistic operating conditions, namely the *high-temperature receiver* operational mode. The testing results showed the proposed unit to store up to 17.5 kWh of thermal energy in a 10 h charging time, although special attention should be given to the minimization of the heat losses towards the environment.

In essence, this work demonstrates the feasibility and functionality of the proposed storage unit integrated into small-scale solar air Brayton cycles. Through the selection of proper storage and containment materials, the use of cost-effective and durable storage solutions is proved to be possible. This brings added values to cogeneration from small-scale solar air Brayton cycles, as the recovered thermal energy can be time-shifted towards periods of greatest heat demand at the expense of a limited investment cost. Ultimately, the results reported in this work provide evidence for future industrial developments.

## Declaration of Competing Interest

The authors declare that they have no known competing financial interests or personal relationships that could have appeared to influence the work reported in this paper.

## Acknowledgment

The authors would like to acknowledge the financial support from Innovate UK for the project “Solar-Turbo CHP, Semi-Renewable, Grid Independent Micro Combined Heat and Power System” (Ref: 105920) as well as funding from the Technology Innovation Agency (TIA) of South Africa. Furthermore, the authors acknowledge Ms. Nikha Harris, Ms. Sarah Jacob and Mr. Westley Roosendaal for their most valuable contributions during the manufacturing and testing of the experimental setup. The paper was presented and published in the proceedings of the 15th International Conference on Heat Transfer, Fluid Mechanics and Thermodynamics (HEFAT2021), Online, 26 – 28 July 2021

## References


[1] Pietsch A, Brandes DJ. Advanced solar Brayton space power systems. Proc. Intersoc. Energy Convers. Eng. Conf., vol. 2, Publ by IEEE; 1989, p. 911–6. https://doi.org/10.1109/iecec.1989.74577.

[2] B. Dickey, Test results from a concentrated solar microturbine brayton cycle integration, Proc. ASME Turbo. Expo. 3 (2012) 1031–1036, https://doi.org/10.1115/GT2011-45918.

[3] W.G. Le Roux, T. Bello-Ochende, J.P. Meyer, A review on the thermodynamic optimisation and modelling of the solar thermal Brayton cycle, Renew. Sustain Energy Rev. 28 (2013) 677–690, https://doi.org/10.1016/J.RSER.2013.08.053.

[4] A. Crespo, C. Barreneche, M. Ibarra, W. Platzer, Latent thermal energy storage for solar process heat applications at medium-high temperatures – a review, Sol. Energy 192 (2019) 3–34, https://doi.org/10.1016/J.SOLENER.2018.06.101.

[5] Omsop, Optimised microturbine solar power system; D1.2-Report On short term storage testing and, Evaluation. (2021).

[6] B. Zohuri, Advanced nuclear openair-brayton cycles for highly efficient power conversion, Molten Salt React. Integr. Molten Salt React. (2021) 171–196, https://doi.org/10.1016/B978-0-323-90638-8.00005-9.

[7] M.A. Bashir, A. Giovannelli, K.P. Amber, M.S. Khan, A. Arshad, A.M. Daboo, High-temperature phase change materials for short-term thermal energy storage in the solar receiver: Selection and analysis, J. Energy Storage 30 (2020), 101496, https://doi.org/10.1016/j.est.2020.101496.

[8] Cameron HM, Mueller LA, Namkoong D, Mueller LA, Namkoong D. Preliminary design of a solar heat receiver for a Brayton cycle space power system 1972.

[9] W.G. Le Roux, A. Sciacovelli, Recuperated solar-dish Brayton cycle using turbocharger and short-term thermal storage, Sol. Energy 194 (2019) 569–580, https://doi.org/10.1016/j.solener.2019.10.081.

[10] Amsbeck L, Denk T, Ebert M, Gertig C, Heller P, Herrman P, et al. Test Of a Solar-Hybrid Microturbine System And Evaluation Of Storage Deployment 2010.

[11] P. Klein, T.H. Roos, T.J. Sheer, Parametric analysis of a high temperature packed bed thermal storage design for a solar gas turbine, Sol. Energy 118 (2015) 59–73, https://doi.org/10.1016/J.SOLENER.2015.05.008.

[12] Wet GJ De, Roux WG, Madani SH, Azadi A, Hosseini S, Craig KJ. Transient Modelling Of Solar-Gas Hybrid Brayton Cycle For Prototype Experimental Setup 2021.

[13] W.B. Stine, R.W. Harrigan, Solar energy fundamentals and design (1985), https://doi.org/10.2172/1000951.

[14] M. Ozturk, I. Dincer, N. Javani, Thermodynamic modeling of a solar energy based combined cycle with rock bed heat storage system, Sol. Energy 200 (2020) 51–60, https://doi.org/10.1016/J.SOLENER.2019.03.053.

[15] K.G. Allen, Performance characteristics of packed bed thermal energy storage for solar thermal power plants, University of Stellenbosch, 2010. PhD thesis.

[16] K. Mohammadi, J.G. McGowan, M. Saghafifar, Thermoeconomic analysis of multi-stage recuperative Brayton power cycles: part I- hybridization with a solar power tower system, Energy Convers Manag. 185 (2019) 898–919, https://doi.org/10.1016/J.ENCONMAN.2019.02.012.

[17] Sarbu I, Sebarchievici C. A comprehensive review of thermal energy storage. Sustain 2018;10. https://doi.org/10.3390/su10010191.

[18] J. Nelson, N.G. Johnson, P. Doron, E.B. Stechel, Thermodynamic modeling of solarized microturbine for combined heat and power applications, Appl. Energy 212 (2018) 592–606, https://doi.org/10.1016/J.APENERGY.2017.12.015.

[19] Brelih Nejc. How to improve energy efficiency of fans for air handling units n.d. https://www.rehva.eu/fileadmin/hvac-dictio/01-2012/02-2012/how-to-improve-energy-efficiency-of-fans.pdf (accessed May 3, 2022).

[20] C. Roosendaal, J.K. Swanepoel, W.G. Le Roux, Performance analysis of a novel solar concentrator using lunar flux mapping techniques, Sol. Energy 206 (2020) 200–215, https://doi.org/10.1016/J.SOLENER.2020.05.050.

[21] C. Chen, H. Zhang, X. Gao, T. Xu, Y. Fang, Z. Zhang, Numerical and experimental investigation on latent thermal energy storage system with spiral coil tube and paraffin/expanded graphite composite PCM, Energy Convers Manag. 126 (2016) 889–897, https://doi.org/10.1016/J.ENCONMAN.2016.08.068.

[22] A. Kumar, R. Agrawal, An experimental investigation of cylindrical shaped thermal storage unit consisting of phase change material based helical coil heat exchanger, J. Energy Storage 45 (2022), 103795, https://doi.org/10.1016/J.EST.2021.103795.

[23] PCM Products Ltd. PlusICE Range - Sales Literature Brochure 2021. www.pcmproducts.net/Phase_Change_Material_Products.html (accessed December 10, 2020).

[24] P. Royo, V.J. Ferreira, Z. Ure, S. Gledhill, A.M. López-Sabirón, G. Ferreira, Multiple-Criteria Decision Analysis and characterisation of phase change materials for waste heat recovery at high temperature for sustainable energy-intensive industry, Mater. Des. 186 (2020), 108215, https://doi.org/10.1016/j.matdes.2019.108215.

[25] J. Maldonado, M. Fullana-Puig, M. Martín, A. Solé, Á. Fernández, A. de Gracia, L. Cabeza, Phase change material selection for thermal energy storage at high temperature range between 210 °C and 270 °C, Energies 11 (4) (2018) 861.

[26] P.J. Shamberger, N.M. Bruno, Review of metallic phase change materials for high heat flux transient thermal management applications, Appl. Energy 258 (2020), 113955, https://doi.org/10.1016/j.apenergy.2019.113955.

[27] Zhao W, Zheng Y, Sabol JC, Oztekin A, Neti S, Tuzla K, et al. Thermal Energy Storage Using Zinc as Encapsulated Phase Change Material. ASME 2011 Int Mech Eng Congr Expo IMECE 2011 2012;4:849–56. https://doi.org/10.1115/IMECE2011-63988.

[28] Haifa Group n.d. https://www.haifa-group.com/ (accessed March 9, 2021).

[29] Marlyn Chemicals n.d. http://marlyn.co.za/ (accessed March 3, 2021).

[30] R.W. Powell, C.Y. Ho, P.E. Liley, Thermal Conductivity of Selected Mater. (1968), https://doi.org/10.6028/NBS.NSRDS.8.

[31] D. Kearney, U. Herrmann, P. Nava, B. Kelly, R. Mahoney, J. Pacheco, R. Cable, N. Potrovitza, D. Blake, H. Price, Assessment of a molten salt heat transfer fluid in a parabolic trough solar field, J. Sol. Energy Eng. Trans. ASME 125 (2) (2003) 170–176.

[32] COMSOL Multiphysics® Modeling Software n.d. https://www.comsol.com/ (accessed February 24, 2020).

[33] D.C. Wilcox, Turbulence Modeling for CFD. (1993).

[34] S.S.M. Tehrani, R.A. Taylor, P. Saberi, G. Diarce, Design and feasibility of high temperature shell and tube latent heat thermal energy storage system for solar thermal power plants, Renew. Energy 96 (2016) 120–136, https://doi.org/10.1016/j.renene.2016.04.036.

[35] M.J. Moran, H.N. Shapiro, D.D. Boettner, M.B. Bailey, Fundamentals Of Eng. Thermodynamics. (1987).

[36] Manual Comsol Multiphysics Reference. Solving time dependent models with inconsistent initial values - Knowledge Base n.d. https://uk.comsol.com/support/knowledgebase/1172 (accessed March 25, 2020).

[37] Refraline International | Refractory Engineering Solutions n.d. https://refraline.com/contact-us/ (accessed December 22, 2021).

[38] Thermocouples - product overview - WIKA n.d. https://www.wika.com/en-en/thermocouples.WIKA (accessed December 22, 2021).

[39] H.W. Ryu, S.W. Woo, B.C. Shin, S.D. Kim, Prevention of supercooling and stabilization of inorganic salt hydrates as latent heat storage materials, Sol. Energy Mater. Sol. Cells 27 (1992) 161–172, https://doi.org/10.1016/0927-0248(92)90117-8.

[40] N.H.S. Tay, F. Bruno, M. Belusko, Experimental validation of a CFD and an ε-NTU model for a large tube-in-tank PCM system, Int. J. Heat Mass Transf. 55 (2012) 5931–5940, https://doi.org/10.1016/J.IJHEATMASSTRANSFER.2012.06.004.

[41] ARMCO® Pure Iron and Specialty Steels since 1924 | AK Steel Ltd n.d. https://www.aksteel.co.uk/ (accessed February 18, 2021).

[42] Z. Yu, M. Chen, J. Wang, F. Li, S. Zhu, F. Wang, Enamel coating for protection of the 316 stainless steel against tribo-corrosion in molten zinc alloy at 460 °C, J. Mater. Sci. Technol. 65 (2021) 126–136, https://doi.org/10.1016/j.jmst.2020.04.079.

[43] D.K. Johar, D. Sharma, S.L. Soni, P.K. Gupta, R. Goyal, Experimental investigation on latent heat thermal energy storage system for stationary C.I. engine exhaust, Appl. Therm. Eng. 104 (2016) 64–73, https://doi.org/10.1016/J.APPLTHERMALENG.2016.05.060.

[44] I. Ortega-Fernández, J. Rodríguez-Aseguinolaza, Thermal energy storage for waste heat recovery in the steelworks: the case study of the REslag project, Appl. Energy 237 (2019) 708–719, https://doi.org/10.1016/J.APENERGY.2019.01.007.

[45] A. Palacios, M.E. Navarro, Z. Jiang, A. Avila, G. Qiao, E. Mura, et al., High-temperature corrosion behaviour of metal alloys in commercial molten salts, Sol. Energy 201 (2020) 437–452, https://doi.org/10.1016/j.solener.2020.03.010.